


Ultra-wide dual-band Rydberg atomic receiver based on space division multiplexing radio-frequency chip modules



Li-Hua Zhang^{1,2} , Bang Liu^{1,2}, Zong-Kai Liu^{1,2}, Zheng-Yuan Zhang^{1,2}, Shi-Yao Shao^{1,2}, Qi-Feng Wang^{1,2}, Yu Ma^{1,2}, Tian-Yu Han^{1,2}, Guang-Can Guo^{1,2}, Dong-Sheng Ding^{1,2,*} & Bao-Sen Shi^{1,2}

¹Key Laboratory of Quantum Information, University of Science and Technology of China, Hefei 230026, China ²Synergetic Innovation Center of Quantum Information and Quantum Physics, University of Science and Technology of China, Hefei 230026, China

*E-mail: dds@ustc.edu.cn (Dong-Sheng Ding)

Cite as: Zhang, L.-H. et al. Ultra-wide dual-band Rydberg atomic receiver based on space division multiplexing radio-frequency chip modules. *Chip* 3, 100089 (2024). <https://doi.org/10.1016/j.chip.2024.100089>

Received: 3 January 2024

Accepted: 28 March 2024

Published online: 2 April 2024

Detecting microwave signals over a wide frequency range is endowed with numerous advantages as it enables simultaneous transmission of a large amount of information and access to more spectrum resources. This capability is crucial for applications such as microwave communication, remote sensing and radar. However, conventional microwave receiving systems are limited by amplifiers and band-pass filters that can only operate efficiently in a specific frequency range. Typically, these systems can only process signals within a three-fold frequency range, which limits the data transfer bandwidth of the microwave communication systems. Developing novel atom-integrated microwave sensors, for example, radio-frequency (RF) chip-coupled Rydberg atomic receiver, provides opportunities for a large working bandwidth of microwave sensing at the atomic level. In the current work, an ultra-wide dual-band RF sensing scheme was demonstrated by space-division multiplexing two RF-chip-integrated atomic receiver modules. The system can simultaneously receive dual-band microwave signals that span a frequency range exceeding 6 octaves (300 MHz and 24 GHz). This work paves the way for multi-band microwave reception applications within an ultra-wide range by RF-chip-integrated Rydberg atomic sensor.

Keywords: Dual-band, Rydberg, Radio-frequency chip, Atomic receiver, Space-division multiplexing

INTRODUCTION

Microwave electric field sensing is endowed with a wide range of applications, including cosmology detection¹, remote sensing² and communication³. Broadband Microwave reception technology enhances data transfer rates in communication⁴, and improves resolution in imaging and remote sensing⁵. Due to the performance limitations of amplifiers and band-pass filters, typically, conventional receiver systems are designed for a specific frequency range and are unable to effectively handle signals with large frequency spans simultaneously. The upper-frequency limit of a conventional receiver is generally within three octaves. In conventional RF sensing systems, the bandwidth of most amplifiers fails to exceed an octave with high efficiency over the entire operating range due to the overlapping of the fundamental wave of high frequency and the harmonic wave of low frequency. To get the working bandwidth across octaves, engineers have to set the band-edge frequencies to satisfy some conditions and constantly adjust the impedance of the system according to the frequency of the microwave in the sacrifice of efficiency^{6–9}. In contrast, Rydberg atomic antennas have specific advantages in radio frequency (RF) detection, such as high sensitivity^{10–12}, self-calibration¹³, low field perturbation, high accuracy¹⁴, a wide operating frequency range (from direct current (DC) to terahertz) and non-destructive detection, making them free of thermal noise^{15–20}. Besides, the frequency response of Rydberg atoms can be altered and extended by an extra RF field^{21–25}.

Rydberg atoms exhibit unique physical properties such as long coherence time and large polarization rate²⁶, which makes Rydberg atoms sensitive to a wide range of RF signals and strongly coupled to broadband RF signals. Rydberg atoms hold promise in the reception of more information in a broader spectrum resource and enhancing bandwidth. For example, developing multi-band atomic antennas can enhance the spectrum utilization efficiency, increase system capacity, and adapt to different application scenarios^{27–29}. There have been many works in this direction, for example, multi-band amplitude modulation (AM) and frequency modulation (FM) microwave communication³⁰ in a centimeter-sized glass cell, multi-band microwave reception^{30,31} in a

glass cell with two different atomic species of Rubidium and Cesium atoms. By utilizing Rydberg RF transitions with different final states, multi-band reception and communication with inherently different transition frequencies are demonstrated^{32–34}. The integration of the RF metawaveguide chip with the Rydberg sensing system unleashes the high-sensitivity potential of Rydberg atoms and extends the continuous working bandwidth of the atomic receiver. Based on this RF-chip-integrated design, a space-division multiplexing and modular dual-band microwave reception was demonstrated in the current work by detecting RF signals in two atomic receiver modules. The working frequencies in our system can be arbitrarily chosen within the ultra-wideband range of 300 MHz ~ 24 GHz, exhibiting the ability of dual-band microwave processing across six octaves. This space-division multiplexing RF detection method based on RF-chip-integrated atomic receiver modules enables the integration of other microwave components into the system, making the system simple, compact, and scalable.

RESULTS AND DISCUSSION

Experimental setup As the energy-level diagram illustrated by Fig. 1a, the Rubidium atoms were excited from ground state $5S_{1/2}$ to Rydberg state $58D_{5/2}$ through a two-photon electromagnetically induced transparency (EIT) scheme³⁵. The atoms at the Rydberg state $58D_{5/2}$ can be driven by the input LO and signal RF fields with several transitions of $59P_{3/2} \leftrightarrow 58D_{5/2}$, $58D_{5/2} \leftrightarrow 57F_{7/2}$, $56F_{7/2} \leftrightarrow 58D_{5/2}$,

and $58D_{5/2} \leftrightarrow 60P_{3/2}$. For simplicity, only the transitions from $58D_{5/2}$ to the adjacent ($\Delta n = \pm 1$) and the next-adjacent ($\Delta n = \pm 2$) Rydberg state were taken into consideration since their dipole moments are larger than that of other dipole-allowed RF transitions. The frequencies of these transitions are 10.8 GHz, 11.8 GHz, 24.7 GHz, and 25.0 GHz, respectively. The resonant frequencies of these transitions were calculated by the python package³⁶ cover a large range. The Rydberg atomic receiver has an enhanced working bandwidth due to both the resonant and off-resonant coupling with RF fields by the atomic RF transitions mentioned earlier. The effective coupling between RF fields and Rydberg atoms was realized via the (resonant) Autler–Townes (AT) effect and the (off-resonant) AC-stark effect.

Fig. 1b shows the experiment setup of the dual-band microwave reception based on the RF-chip-integrated Rydberg receivers. The single reception module in the experiment consists of a vapor cell and an RF chip below the cell. The structure of a single module and the space-division multiplexing of dual-band detection schemes are given in Fig. 2a. The spoof-surface plasmon polaritons (spoof-SPP) RF chip was utilized to enhance the electric field intensity over the region where Rydberg atoms are excited by the laser beams in a vapor cell with a 50-mm length. The coupling laser (Toptica, DLpro 480) and the probe laser (Toptica, DLpro 780) counter-propagate with each other over the periodical meta-structure on the chip, and the beams were focused in the centimeter-sized vapor cell. Based on the single-reception module, dual-band reception was achieved by sharing the RF signal between the two single modules. Different frequency bands were selectively detected through different LO fields. The free-space LO field E_{LO} beat

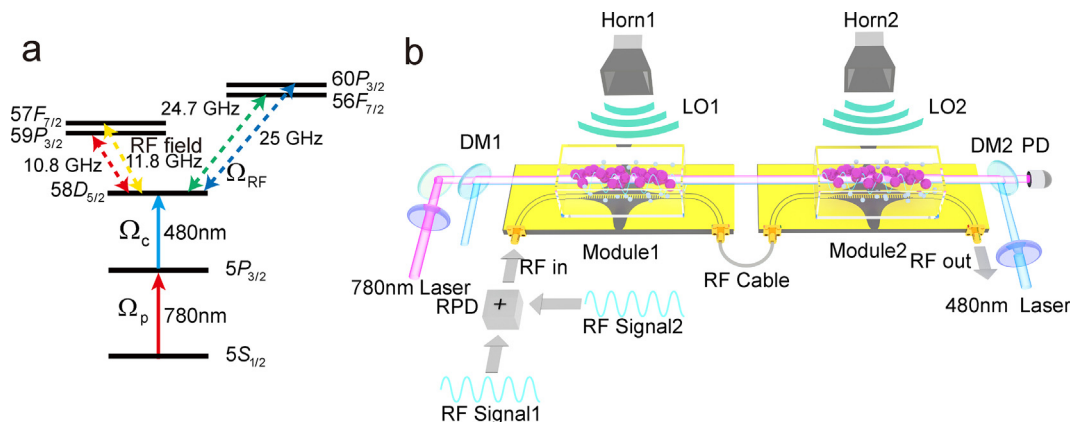


Fig. 1 | Experimental energy-level diagram and setup. **a**, The energy-level diagram of Rb atom (Rubidium 85). The probe and coupling laser beams couple the atomic states of ground state $5S_{1/2}$, intermediate state $5P_{3/2}$, and Rydberg state $58D_{5/2}$ to realize electromagnetically induced transparency (EIT) configuration. The RF fields can couple the Rydberg state $58D_{5/2}$ with its adjacent Rydberg states $59P_{3/2}$, $57F_{7/2}$, $56F_{7/2}$, and $60P_{3/2}$, with different frequency intervals of 10.8 GHz, 11.8 GHz, 24.7 GHz, and 25.0 GHz (dashed arrows), respectively. The coupling between the RF fields from 300 MHz to 25 GHz and Rydberg atoms can be separated into off-resonant and resonant regimes. For the RF fields with frequencies far from resonance, a strong local oscillator (LO) RF field is required to increase the system response, in which the AC-stark shifts induced by several pairs of Rydberg states off-resonant coupling. Near the resonant regime, the RF fields at frequencies 10.8 GHz, 11.8 GHz, 24.7 GHz, and 25 GHz drive Rydberg states with Autler–Townes (AT) effect. **b**, The multi-band microwave fields reception experiment setup. The whole detection system is composed of two receiver modules; each module consists of an RF chip and a centimeter-sized glass cell. A 780-nm probe laser and a 480-nm coupling laser are input into the two cells together with a dichroic mirror (DM). Then the EIT transmission signal of the probe laser is collected by a photodetector (PD). The information of RF signals (RF Signal1 and RF Signal2) can be read from the EIT spectrum output from the PD. Rydberg atoms are responded by the RF fields radiated by the LO field from the microwave horn and the signal field on the spoof-surface plasmon polaritons (spoof-SPP) chip. This supports an arbitrary tunable dual-band detection by using a pair of space-division multiplexing RF-chip-integrated Rydberg receivers. The reception frequencies can be altered by changing the frequencies of the two strong LO fields emitted from the two microwave horns. Two RF signals (RF Signal1 and RF Signal2) with different frequencies are combined with a resistance power divider (RPD) and then input to the chip port. Abbreviation: RF, radio frequency.

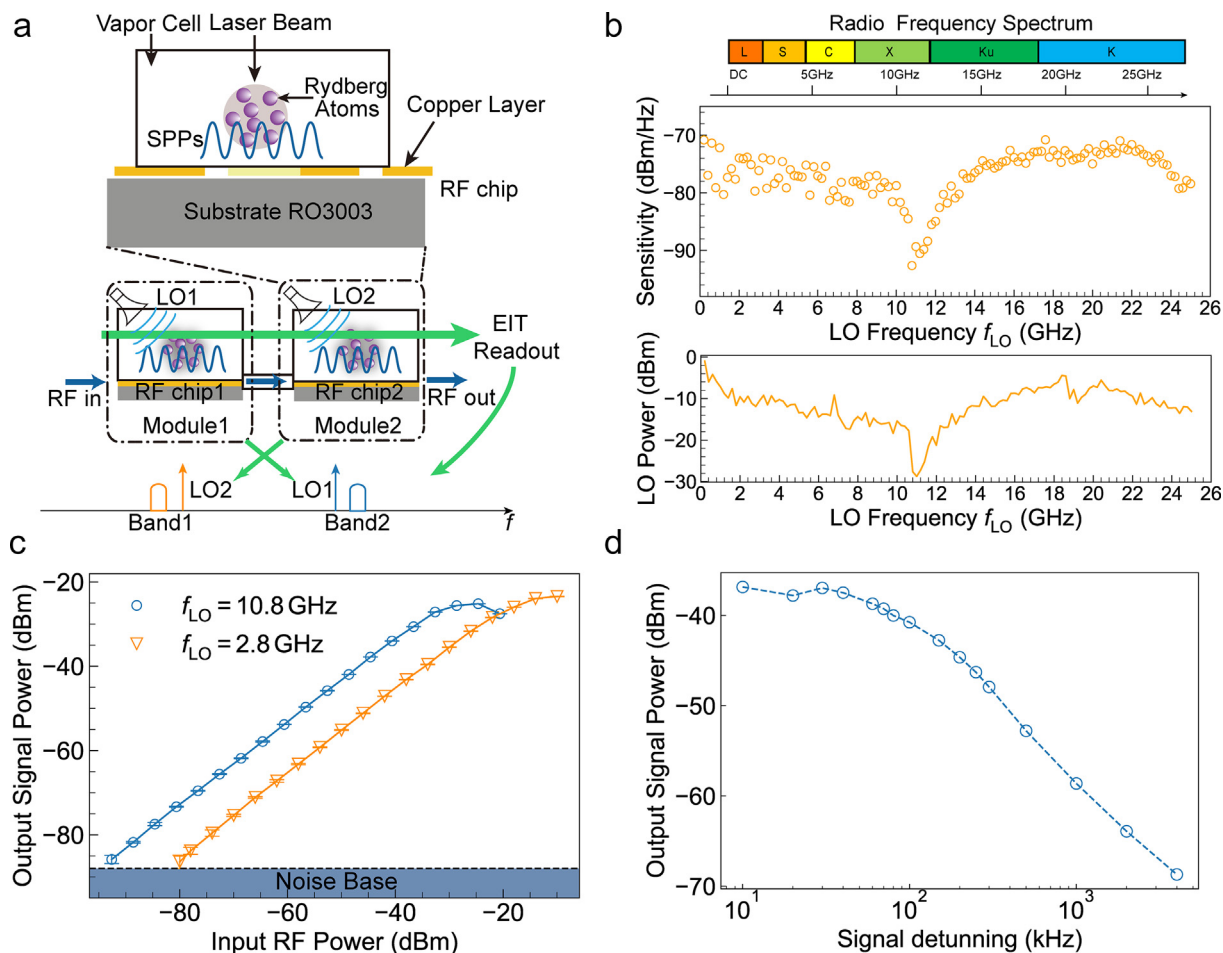


Fig. 2 | The performance of the single RF-chip-integrated Rydberg atomic receiver module. **a**, The structure of the RF-chip-integrated Rydberg atomic receiver. The integrated structure contains a spoof-surface plasmon polaritons (spoof-SPP) chip and a centimeter-sized glass cell. Over the chip surface, the RF signals in SPP mode are coupled with Rydberg atoms, and then the output signals are detected in an atomic heterodyne scheme by imposing LO fields with different frequencies. **b**, The intrinsic sensitivity for the RF-chip-integrated Rydberg system after a correction of the insert loss is plotted with red circles. Each datapoint is acquired with a frequency separation of 200 MHz. At 10.8 GHz, the maximum sensitivity is measured at about -93 dBm/Hz. In other frequencies (off-resonant region) above 300 MHz, the sensitivity varies from about -70 dBm/Hz to -80 dBm/Hz. The detection range of the RF-chip-integrated Rydberg system covers the RF band from low frequency to K-band (300 MHz–25 GHz). The optimized LO field power applied for each frequency is plotted in Fig. 2b, which varies from near 0 dBm to -29 dBm with the LO frequency. The power of the LO field has a similar variation tendency as that of the system sensitivity. **c**, The system dynamic range at 2.8 GHz (blue circle) and 10.8 GHz (orange triangles). The output signal varies in a similar range from about -25 dBm to -86 dBm (equal to the system noise base), the resonant sensitivity at 10.8 GHz is about 13 dB larger than the off-resonant situation at 2.8 GHz. The error bars come from experimental statistics. **d**, The system instantaneous bandwidth. We scan the signal RF detuning δ_{sig} from the LO field ($f_{\text{LO}} = 2.8$ GHz), and set the power of the signal RF field to -25 dBm (About -28 dBm at the input port). The instantaneous bandwidth of the system is about 100 kHz at a 3 dB reduction. Abbreviations: LO, local oscillator; RF, radio frequency.

with the RF signal field E_{sig} over the chip and the output beat signal with a frequency of $\delta_{\text{sig}} = |f_{\text{sig}} - f_{\text{LO}}|$ was read from the Rydberg EIT spectrum with a photodetector (Thorlabs, PDA36A).

Ultra-wide working bandwidth Arbitrarily tunable RF working points are required by the dual-band microwave reception experiment. This could be achieved by off-resonant atomic heterodyne method^{15,16,18,21}. For the operation of the Rydberg atomic receiver under off-resonant conditions, the response of Rydberg atoms to the off-resonant RF signal is improved by applying a strong LO field. The strong LO field couples many adjacent Rydberg states with the initial Rydberg state $58D_{5/2}$ and induces strong AC-stark energy shifts on the energy levels of Rydberg atoms. The weak RF signal beats with the LO

field by perturbing the total RF field sensed by the atoms. Finally, the amplitude and phase of the signal RF field are read from the beat signal of the Rydberg EIT spectrum. In our experiment, the frequencies of the strong LO RF field and signal RF field were scanned from 300 MHz to 25 GHz, and the detuning of the signal RF field from the LO field $\delta_{\text{sig}} = |f_{\text{sig}} - f_{\text{LO}}|$ was set to 20 kHz at each tested frequency point. The output beat signal amplitude for the EIT-AT spectrum was then recorded to calculate the intensity of the input weak-signal RF field. To estimate the sensitivity of the system, the insertion loss of coaxial cables and a resistance power divider are needed to be calibrated, which is shown in Fig. 1b. The sensitivity is obtained based on the beat-note response in the linear region and is in inverse ratio to the photodetector noise.

To ensure the accuracy of the measurement, the input power of the RF signal field was set within the linear zone of the atomic heterodyne response. The sensitivity of the system was found to be lower below 300 MHz compared to the range of 300 MHz to 25 GHz. This is attributed to manufacturing errors of the spoof-SPP chip as indicated by the S21 parameter, details can be seen in the Method Section. At low RFs, the propagation constant of the SPP surface wave is reduced, leading to weak field confinement over the spoof-SPP structure. In addition, the screening effect of the vapor cell leads to a decrease in the intensity of RF fields in the range of a few kHz³⁷, whereas at frequencies above 300 MHz, the system tends to show obvious enhancement when the RF fields resonate with the Rydberg transitions. Due to the similar coupling strength of Rydberg atoms with the RF field (either at 10.8 GHz and 11.8 GHz or at 24.7 GHz and 25 GHz) and the fluctuation of the chip performance, it is of great difficulty to distinguish all the four resonant peaks for Rydberg atoms in Fig. 2b. Two resonant peaks are observed at approximately 10.8 GHz and 25 GHz. At 10.8 GHz, the maximum (input) sensitivity of the system is around -93 dBm/Hz. Although there is a resonant response at 25 GHz due to the resonant transition, it is relatively weaker than the 10.8-GHz peak due to the reduction of the transition strength and spoof-SPP chip loss. The system sensitivity of the single module below 11 GHz has more fluctuations, which is partly ascribed to the uneven conversion for electric field intensity of the chip at a lower frequency. The RF transitions of ($55F_{7/2} \leftrightarrow 58D_{5/2}$ and $58D_{5/2} \leftrightarrow 61P_{3/2}$) cover the frequencies 60 GHz (59.001 GHz and 63.218 GHz), these frequencies are far away from the frequency of the input RF field. Due to the larger detuning of the RF fields with transitions $55F_{7/2} \leftrightarrow 58D_{5/2}$ or $58D_{5/2} \leftrightarrow 61P_{3/2}$, the AC-stark shift for the Rydberg states $55F_{7/2}$ and $61P_{3/2}$ is small. In addition, the degradation of chip performance also contributes to a decrease in system sensitivity above 25 GHz. The utilization of lower- n Rydberg energy levels to increase the off-resonant response range of Rydberg atoms and the optimization of the metawaveguide structure may facilitate further improvement of the system's operating range.

However, the utilization of lower- n Rydberg states may introduce weaker off-resonant and resonant sensitivity due to their smaller polarizability and dipole transition moment. Different optimal LO powers were applied for LO frequencies near resonance and far from resonance to maximize the output signal, as shown in Fig. 2b. At 10.8 GHz, the power was set to -29 dBm. Furthermore, in the off-resonant heterodyne scheme ($\Delta_{\text{RF}} \gg \Gamma_{\text{EIT}}$, where the RF signal detuning is larger than the EIT bandwidth), a LO field much larger than that in the resonant scheme is required. Nevertheless, the field enhancement feature of the spoof-SPP chip helps to increase the coupling strength between the RF fields and Rydberg atoms and therefore alleviates the power requirement for the LO field, which enables the optimal operation under off-resonant conditions. This, in turn, reduces the energy consumption of the system, thus facilitating further miniaturization.

The dynamic range and instant bandwidth of the single receiver The dynamic range and instantaneous bandwidth of the RF-chip-integrated Rydberg atomic receiver determine how weaker and how much signal can be received. The dynamic range of a dual-band receiver refers to the difference in signal strength that it can simultaneously handle, ranging from the maximum to the minimum. The total dynamic range of our system is about 70 dB, and a linear dynamic of about 60 dB is shown in Fig. 2c at a 1-Hz-resolution bandwidth measured by the electric spectrum analyzer. The sensitivity and dynamic range are finally limited by a noise base of about -90 dBm from the optical read-

out. In the measurement of dynamic range, the LO and signal RF fields were firstly combined by a resistance power divider and subsequently fed into the spoof-SPP chip. The signal dynamic range for the RF signals in different frequency bands was individually tested but not input together. The dynamic achieved here is not the cutting-edge, which is mainly due to the low coupling laser power. Further improvement of the dynamic range of the system can be achieved by increasing the Rydberg excitation efficiency with a stronger coupling laser system to increase the EIT signal intensity or locking lasers to a reference ultra-stable cavity to reduce the read-out noise¹⁰.

The instantaneous bandwidth of a receiver refers to the frequency range that the receiver can simultaneously process at a given moment, referring to the simultaneous signal-frequency reception range and processing capability of the receiver. By inputting the signal RF field with detuning δ_{sig} from the LO RF field ($f_{\text{LO}} = 2.8$ GHz), the instantaneous bandwidth of the system can be measured. The results are given in Fig. 2d, in which an instantaneous bandwidth of about 100 kHz is obtained. The bandwidth is ultimately limited by the Rydberg-EIT bandwidth, which is close to 10 MHz. Therefore, the bandwidth for the system can be further optimized by reducing the beam waists (focusing the lasers beams) or adjusting the coupling and probe laser powers³⁸. Although a relatively small instantaneous bandwidth of about 100 kHz is obtained in the current experiment, there are also some potential applications in which the reception of narrowband signals is required, such as RF identification and navigation systems. In these cases, the receivers work with smaller instantaneous bandwidth. The instantaneous bandwidth could exceed 10 MHz working in a six-wave mixing scheme³⁹.

Dual-band atomic microwave reception based on space-division multiplexing Distinct from conventional receivers based on absorption detection, the EIT-based Rydberg atomic RF sensor can detect the RF field with a little perturbation to the input signal^{15,18}, thus a dual-band multi-channel detection can be achieved by space-division multiplexing two chip-integrated modules. After the characterization of the ultra-wide working bandwidth of the RF-chip-integrated Rydberg receiver, RF-signal reception with tunable dual-band frequencies was performed with the adoption of two modules (module 1 and module 2, as shown in Fig. 1b and 2a). These two modules are spatially separated but connected with a low-loss RF cable. Heterodyne detection was also applied in this case, but here the LO RF fields were applied in free space by a pair of horn antennas to reduce the crosstalk between the LO fields in a space-division multiplexing scheme (in principle, the LO RF fields can be fed through the chip ports directly, but the energy shift of the two strong LO fields would couple with Rydberg atoms in the same vapor cell and influence the optimal working point for each module). Due to the low-perturbation feature of the Rydberg atomic receiver, module 1 rarely affects the RF signal detected by module 2. Module 1 only causes a small reduction of the sensitivity for module 2 due to the small transmission loss (which is mainly determined by the transmission coefficient of the single RF chip). Based on this advantage, a tunable dual-band RF detection can be achieved by only monitoring the probe beam after module 2. The minimum frequency separation at which the two modules can work without affecting each other is of the same order of magnitude with the EIT bandwidth (about 10 MHz). As the system is operated mainly under off-resonant conditions, the dispersion and absorption of the RF signal by the previous module (module 1) is small. However, the leakage of a strong off-resonant LO field between the modules is measurable. Therefore, the separation of the operation frequencies between the two modules needs to be much larger than the system's instantaneous bandwidth (100 kHz) so

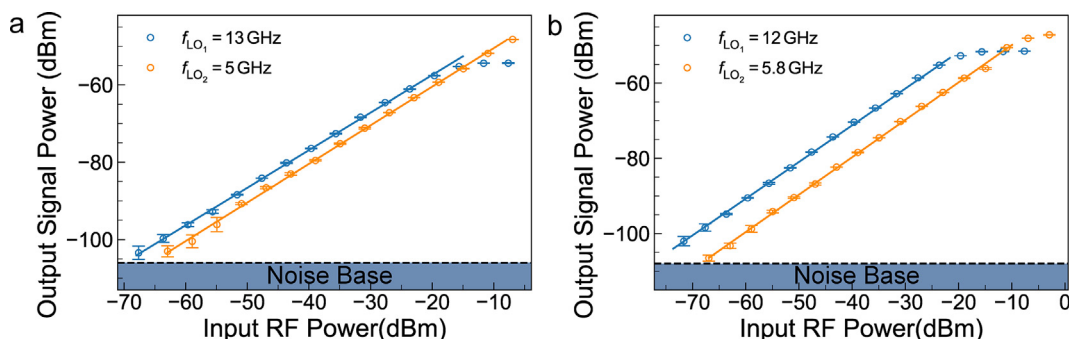


Fig. 3 | The dynamic range for dual-band microwave reception. RF signals at arbitrarily selected frequencies (5 GHz and 13 GHz, 5.8 GHz, and 12 GHz) are received, and the corresponding dynamic ranges are plotted. **a**, The input RF signal with a frequency of $f_{\text{sig}} = 5 \text{ GHz} + 20 \text{ kHz}$, and $f_{\text{sig}} = 13 \text{ GHz} + 20 \text{ kHz}$; the linear dynamic ranges are about 57 dB at 5 GHz and 55 dB at 13 GHz **b**, The dynamic ranges are about 56 dB at 5.8 GHz and 52 dB at 12 GHz. The error bars come from experimental statistics. Abbreviation: RF, radio frequency.

as to minimize the crosstalk between the modules. In order to reduce the insert loss of the system to receive the dual-band RF fields, module 1 is applied to detect the signal above the 10 GHz, and module 2 adopted to receive the signal below 10 GHz. The spoof-SPP chip has a less loss of below 10 GHz, for example, the total insert loss measured for the signal at 5.8 GHz (containing the loss of the first chip and the RF cable) is about

1.65 dB. The dynamic range and the output signal power of the dual-band RF-chip-integrated Rydberg receivers are plotted and shown in Fig. 3a. The frequency of the LO field of module 1 f_{LO_1} is set to 5 GHz and the frequency of module 2 f_{LO_2} set to 13 GHz in Fig. 3a to receive RF signals with an offset of 20 kHz from LO fields, and in Fig. 3b, f_{LO_1} is set to 13 GHz and f_{LO_2} set to 5.8 GHz.

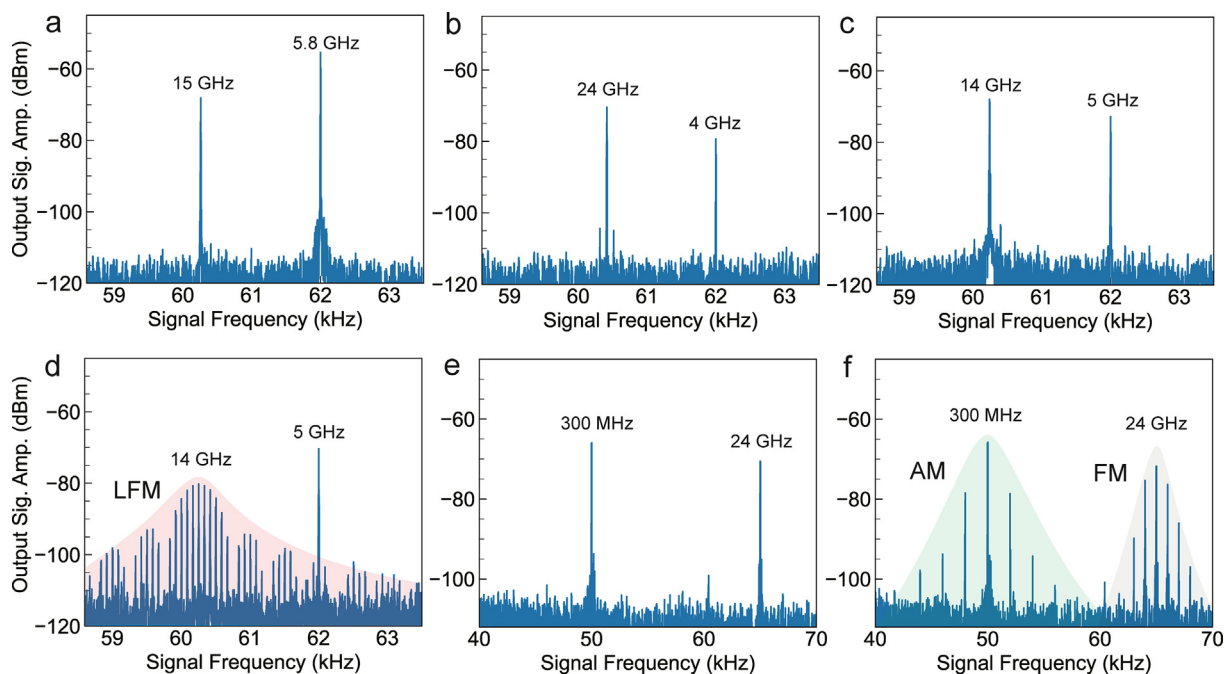


Fig. 4 | The arbitrary dual-band signal spectrum received simultaneously in two serial RF-chip-integrated atomic receiver modules. **a–f**, The high frequencies of the LO fields (applied to module 1) f_{LO_1} are set to 15 GHz, 14 GHz, and 24 GHz, and the low frequencies of the LO fields (applied to module 2) f_{LO_2} are set to 5.8 GHz, 5 GHz, 4 GHz, and 300 MHz. **c**, The frequency spectrum for the input signals with central frequencies of 14 GHz and 5 GHz. **d**, The frequency spectrum for the input signals with the same central frequencies but with a linear frequency modulation applied on the 14-GHz signal (LFM, marked by red shaded area). In these measurements, the RF signal with a frequency offset of $\delta_{\text{sig}} = 60.2 \text{ kHz}$ and 62 kHz from the corresponding LO signal are received by two atomic sensor modules. **e–f**, The frequency spectrum for simultaneously receiving at 0.3 GHz and 24 GHz, in which amplitude modulation (AM, marked by green shaded area) and frequency modulation (FM, marked by gray shaded area) are applied to the RF carrier with frequencies of 0.3 GHz and 24 GHz (**f**). In these measurements, the RF signal with a frequency offset from the LO field δ_{sig} is set as 50 kHz and 65 kHz. All of the spectra are sampled by an electric spectrum analyzer (Ceyear 4024F) with an RBW (and VBW) of 3 Hz and a sweep time of 3.277s in sweep mode. Abbreviations: LO, local oscillator; LFM, linear frequency modulation; RBW, resolution bandwidth; RF, radio frequency; VBW, video bandwidth.

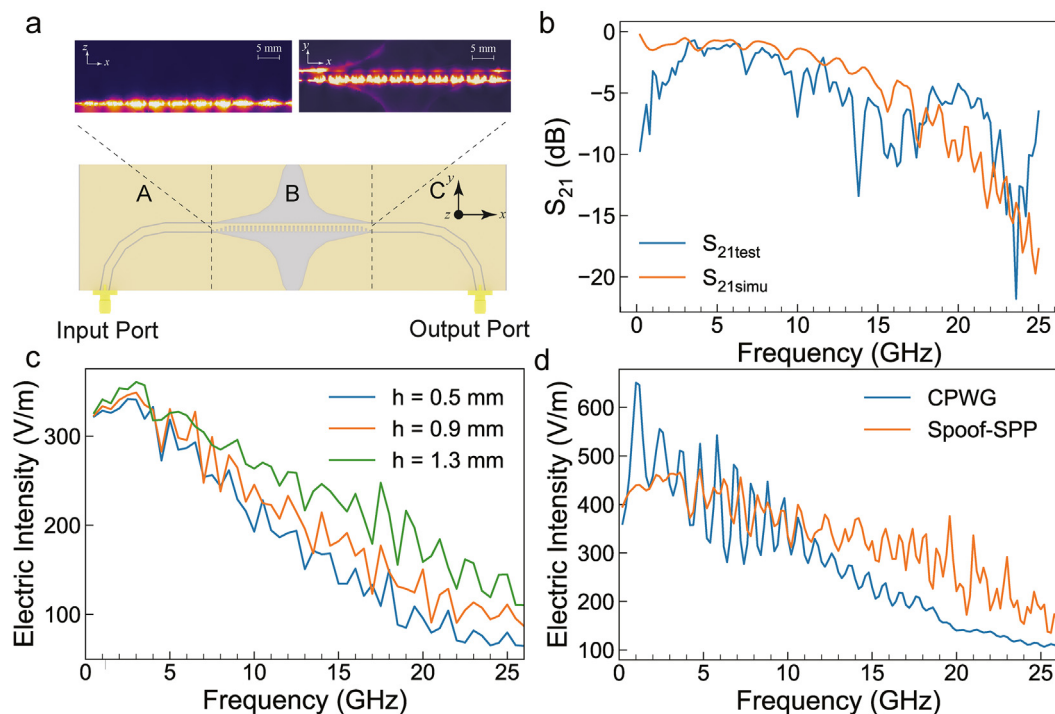


Fig. 5 | The properties of the spoof-SPP chip. **a**, The structure of the spoof-SPP chip and the steady field intensity distribution in xz and xy surface over the spoof-SPP region with an RF signal with a frequency of 18-GHz input. The RF field transmits through the region of A, B, and C on spoof-SPP chips with quasi-transverse electromagnetic (TEM) mode, SPP, and quasi-TEM modes. **b**, The experimental tested and simulated results of S_{21} parameters for the chip. **c**, The simulated averaged electric field intensity over the chip surface for different groove depths h of spoof-SPP structure are plotted. **d**, The simulated intensities of the electric field for the CPWG in ref.¹⁸ and spoof-SPP in this article are illustrated. In these simulations, the power at the input port of the chip is set to be 20 mW. The region where the electric field strength is averaged is cylindrical. The radius of this region is 0.3 mm, and the length is 50 mm. Abbreviations: CPWG, coplanar waveguide with ground; RF, radio frequency; spoof-SPP, spoof-surface plasmon polaritons.

In the current experiment, there is a sensitivity reduction of about 10 dB compared to the single-module scheme in which the LO and signal RF fields are put together through the same input port; This is mainly resulted from the mismatches between the SPP fields over the chip and the free-space field from the horn antenna. The mode of the LO field emitted from rectangular waveguide antenna is the transverse electric (TE) mode, whereas the SPP-mode RF field propagating on the chip does not match the TE mode in the interaction with Rydberg atoms. This mismatch can be corrected by further technical upgrades such as adding more chips to replace the microwave horn.

The power of the LO RF fields for 5.8 GHz and 5 GHz being input to the horn antenna is about 4 dBm, which is about 15 dB larger than that of the LO RF field directly input through the spoof-SPP chip port. Considering the strong LO field applied to the receiver module, the multi-path diffraction and reflection of the LO field will increase the phase noise of the output signal and reduce the sensitivity of the system⁴⁰. Integrating the wave-absorption material into the reception module and optimizing the metal structure of the chip may facilitate the reduction in the diffraction and reflection effect. Also, this effect will be suppressed if the LO field is applied by another chip efficiently from another side of the vapor cell. Fig. 4 depicts the output frequency spectrum of module 1 and module 2 under dual-band reception at different arbitrary frequencies. This spectrum was recorded by setting the RF signal detuning from corresponding LO fields δ_{sig} to 60.2 kHz (module 1) and 62 kHz (module 2), respectively. The dual-band signal

reception at three arbitrary chosen dual frequencies is demonstrated. The frequencies being chosen are 15 GHz and 5.8 GHz (Fig. 4a), 24 GHz and 4 GHz (Fig. 4b), and 14 GHz and 5 GHz (Fig. 4c). The results show the system's ability to receive dual-band signals simultaneously. The input signal power before module 1 is about -35 dBm, -30 dBm, and -20 dBm for 4 GHz, 5 GHz, and 5.8 GHz, respectively. All the power of these signals was measured with the adoption of a frequency analyzer (Ceyear, 4024F).

In addition, dual-band simultaneous reception with different modulations for each RF signal is also demonstrated. In the current work, different frequency modulations were set for the two modules by applying a linear frequency modulation for module 1 (with a center frequency of 14 GHz) and applying a single frequency (5 GHz) for module 2. The results are given in Fig. 4d. Many modulation sidebands are observed around 14 GHz, whereas only a single narrow peak appears at 5 GHz. This result is in good agreement with the modulation. We also demonstrate RF receiving with a large range of 300 MHz and 24 GHz; the results are shown in Fig. 4e and f. As shown in Fig. 4f, the RF signals with different modulations and different central frequencies are received simultaneously (300 MHz and 24 GHz). Thus, the spectrum information in two bands is captured, which means that a faster data reception rate is achieved than the single-reception module. For a single-receiver module, only the RF signal in a certain band (either near 300 MHz or 24 GHz) is received. Here, the RF signal at 300 MHz is amplitude modulated (AM) with a modulation frequency of 2 kHz and

the RF signal at 24 GHz is frequency modulated (FM) with a modulation frequency of 1 kHz. This dual-band RF reception across six octaves shows the multi-band information processing ability of the RF-chip-integrated Rydberg atomic device.

DISCUSSION

The power sensitivity of the chip system is mainly limited by the electric field response and the coupling strength between Rydberg atoms and the RF chip. As Rydberg atoms have a direct response to the electric field strength and are excited through a non-absorptive detection process, it is necessary to convert the power sensitivity of an RF signal to the intrinsic electric sensitivity of Rydberg atoms⁴¹. A field enhancement scheme can be adopted to improve the coupling strength between the atoms and the different RF signals, which improves the overall performance compared to a simple free-space-sensing scheme^{42,43}. In addition, the multi-band RF field enhancement devices incorporating metal components such as waveguides or resonators may introduce additional thermal noise or bandwidth limitations to the Rydberg sensing system^{44,45}. In our scheme, Rydberg atoms in different modules participate in the reception of fields at different frequencies, thus reducing direct crosstalk between Rydberg atoms.

By integrating the RF field, Rydberg atoms, and optical field on a chip, the sensing system can be made more portable, affordable, and accessible for various applications. The chip sensor in this work without larger vacuum chambers exhibits a more simplified sensor. This multi-band integrated scheme can incorporate various functional modules on the RF chip to realize multiple sensing applications. This integration also allows for compact and lightweight designs, reduces the power requirement for a strong LO field in Rydberg heterodyne sensors benefiting from the field enhancement setup, and minimizes overall costs. One can integrate a large number of RF-chip-integrated Rydberg receivers to demonstrate a sensor array in which each integrated Rydberg receiver could implement a distinct function. Through this method, multiple Rydberg atoms can participate in the measurement compared to the single-module scheme providing extra gain of the sensitivity. Besides, the sensing module in the system is easily extensible due to the simple setup, and the signal for each module can be read out individually and conveniently if fiber-coupled cells are used. In this case, a faster data reception rate than that with the single atomic receiver can be achieved. Notice that a low-noise RF amplifier before the input port may help to largely improve the sensitivity¹⁸; however, extra thermal noises would finally limit the system performance to the thermal noise limitation (-174 dBm/Hz). With the quick improvements in the sensitivity of the Rydberg atomic electrometry⁴⁶ and the combination of the field-enhanced scheme, the thermal noise limitation for the conventional receiver can be beaten^{47,48}.

CONCLUSION

In the current work, multi-band microwave reception was experimentally investigated with the adoption of RF-chip-integrated Rydberg receivers. These receivers can operate across a wide frequency range from 300 MHz to 24 GHz, enabling the measurement of microwave signals in multiple frequency bands simultaneously. The Rydberg receivers with integrated RF chips are capable of simultaneously receiving and processing multiple frequency bands using a single device. A dual-band RF signal that covers a frequency range exceeding six octaves is received by the RF-chip-integrated Rydberg receivers, in which the AM

and FM modulation signals at the different frequency bands are successfully obtained. By integrating the functionalities of both the chip and atoms into a single device, the complexity of the multi-band atomic sensors was reduced, and there is potential for the development of compact and highly integrated systems.

Traditional RF-chip-integrated receivers are designed for specific frequency bands, requiring separate devices for each band, low-noise amplifiers, and complex filters that bring extra thermal noise and frequency restrictions. In contrast, multi-band microwave reception based on Rydberg receivers can cover multiple bands with a single device, thus improving the receiving efficiency.

This is especially important in wireless communications and radar systems, where signals span multiple frequency bands, and the simultaneous reception of multi-band signals allows for parallel processing of signals, thus improving the overall system performance. The reported results show that a new-type continuous-tuning dual-band RF reception by the Rydberg atomic system is modularized and scalable, which is promising for communications and metrology.

METHODS

Design and characterization As the spoof-SPP waveguide cannot be fed efficiently from the Sub-Miniature A (SMA) port, a curved coplanar waveguide (CPW) line is introduced. As shown in Fig. 5a, a gradient transition structure in region B is adopted to finish the mode conversion from the CPW line to the spoof-SPP line⁴⁹. The chip is plated with a 35- μ m copper layer on the Rogers 3003 substrate.

As the output signal of the system depends on the electric intensity of the RF signal sensed by Rydberg atoms^{10,14,18}, the average field intensity over the chip was simulated by the finite element methods. Besides, the transmission coefficients (S21) for the chip were also simulated and experimentally tested, which is shown in Fig. 5b. The difference between the simulation and experimental results of the S21 parameter is mainly ascribed to the fabrication error and the permittivity change of the vapor cell wall compared with the simulated air media. The dispersive property of the SPP wave can be tuned by the groove depth h , and a larger h leads to a lower cut-off frequency. The groove depth h is set to 1.3 mm to balance the wide-band transmission and the constraint ability of the electric field.

The simulation results of the average electric field intensity at a distance of 1 mm above the chip, in a cylindrical region with a radius $r = 300$ μ m, are depicted in Fig. 5c. It is proved that a deeper groove depth facilitates the increase of the field intensity over the chip. Further design optimization is necessary to minimize loss, enhance electric field concentration, and improve detection sensitivity.

At the same time, the coupling loss between the chip and atoms needs to be taken into consideration. This loss is primarily composed of two factors. Firstly, there is a mismatch between the region where the atoms are shinned and the volume where the RF field is concentrated. Secondly, a portion of the SPP wave propagates in the substrate, resulting in the fact that the electric field is not coupling with the atoms. As a result, a part of the effective RF power is lost when it is converted into electric strength on the chip surface.

Simulation of the electric field conversion for the chip The electric field intensity over the chip was simulated by the finite element method. The average electric field over the chip in a cylinder with a radius of 300 μ m for different groove depths was simulated and plotted. Here, our simulation is based on a steady-state solver, so the time-average effect for the electric intensity is considered to be the space averaged due to

the periodical distribution of the RF field. Furthermore, a time-dependent transient analysis may be more accurate about the averaged field intensity.

The average field intensity against frequencies for both the coplanar waveguide (CPW) in ref.¹⁸ and the spoof-SPP chip in the current work are simulated and compared. As shown in Fig. 5d, the CPW has a more effective concentration below 5 GHz since the SPP mode is not perfectly matched, but the variation against the frequency is greater than that against the spoof-SPP chip. The spoof-SPP chip exhibits a slower degradation of the performance and better field-enhancement features above the 10 GHz than the CPW as well as a better field-enhancement performance above 10 GHz. The simulated electric field intensity exhibits a small reduction at low frequency (below 2 GHz).

Besides, the vapor cell causes a significant index-change effect for the RF field over the chip, which needs to be taken into consideration. The Rydberg vapor in the cell has a small index change compared to other components in the reception module. However, there appears an index change of the RF field from glass wall of the vapor cell¹⁵, which leads to a change in polarization and a reduction in the strength of the RF field. Using low-dielectric glass materials⁵⁰, embedding the chip in a larger vapor cell¹⁸ or reducing the thickness of the glass wall are effective ways to suppress this effect, and a finite element simulation including the vapor cell over the chip will reveal more details.

Experiment details The probe beam with a power of 15 μW , which is emitted from a 780-nm diode laser (Toptica, DL pro), has a Rabi frequency of $\Omega_p = 6.62$ MHz (for each probe beam). The probe laser is locked to the atomic transition $^{85}\text{Rb } F = 3 \rightarrow F' = 4$. The coupling beam with a power of 80 mW and $\Omega_c = 9.94$ MHz, which is generated from a 480-nm diode laser (Toptica, DL pro). The coupling laser is resonant with the atomic transition to maximize the read-out signal. The gain of the photodetector is set to different gain levels 10^5 V/A and 10^6 V/A, resulting in a different system noise base of Fig. 2c and Fig. 3.

To measure the properties of a single module of RF-chip-integrated Rydberg receiver, for example, sensitivity, dynamic range, and instantaneous bandwidth, a strong LO RF field and a weak signal RF field (about -35 dBm at the signal source) were firstly combined by a power divider and then fed into the metawaveguide chip through an SMA connector port. Afterwards, the SPP waves of these RF fields were encouraged in the center of the chip (over the spoof-SPP units) and coupled with the excited Rydberg atoms. The probe and coupling beams over the chips were aligned close to the surface of the chip and aligned with the propagation direction of the RF signal. The position for the laser beams in the y-axis direction in Fig. 5 was carefully adjusted to overlap with the center of the slot structure, which has the most uniform and the strongest field distribution over the chip to reduce the inhomogeneous effect of the RF field distribution. The phase and intensity of the traveling wave over the chip vary quickly, so the electric field that is finally detected by the atoms is averaged. In our system, the beams are about 1 mm above the chip.

The LO RF fields in multi-band receiving test (marked as LO1 and LO2) were firstly emitted by two signal sources (Rohde & Schwarz SGS100A and Ceyear 1465F) and then applied through a pair of horn antennas (HD-70WCAS, HD-180SGAH20S) instead of directly injecting to the input port of the chip so as to reduce the crosstalk of the LO RF fields between the two receiving modules. The LO power being input into the horn antennas was set to about 20 dBm for 300 MHz as the frequency had exceeded the working bandwidth for the horn. A larger LO power would significantly broaden the EIT spectrum, thus reducing the

signal–noise ratio. In this process, two signal RF fields were synthesized by two (Rigol DSG3136B and Ceyear 1465F) microwave signal sources.

REFERENCES

- Spitler, L. G. et al. A repeating fast radio burst. *Nature* **531**, 202–205 (2016). <https://doi.org/10.1038/nature17168>.
- Wooster, M. J. et al. Satellite remote sensing of active fires: history and current status, applications and future requirements. *Remote Sens. Environ.* **267**, 112694 (2021). <https://doi.org/10.1016/j.rse.2021.112694>.
- Du, K.-L. & Swamy, M. N. *Wireless Communication Systems: From RF Subsystems to 4G Enabling Technologies*. (Cambridge University Press, 2010). <https://doi.org/10.1017/CBO9780511841453>.
- Busari, S. A., Mumtaz, S., Al-Rubaye, S. & Rodriguez, J. 5G millimeter-wave mobile broadband: performance and challenges. *IEEE Commun. Mag.* **56**, 137–143 (2018). <https://doi.org/10.1109/MCOM.2018.1700878>.
- van Dorp, P., Ebeling, R. & Huizing, A. G. High resolution radar imaging using coherent multiband processing techniques. In *2010 IEEE Radar Conference*, 981–986 (IEEE, 2010). <https://doi.org/10.1109/RADAR.2010.5494478>.
- Wang, C.-X. et al. Cellular architecture and key technologies for 5G wireless communication networks. *IEEE Commun. Mag.* **52**, 122–130 (2014). <https://doi.org/10.1109/MCOM.2014.6736752>.
- Xuan, X., Yang, F. & Liu, C. Design of multioctave high-efficiency power amplifier based on extended continuous Class-B/J modes. *Int. J. RF Microw. Computer-Aided Eng.* **29**, e21899 (2019). <https://doi.org/10.1002/mmce.21899>.
- Zheng, S. Y., Liu, Z. W., Zhang, X. Y., Zhou, X. Y. & Chan, W. S. Design of ultrawideband high-efficiency extended continuous class-F power amplifier. *IEEE Trans. Ind. Electron.* **65**, 4661–4669 (2018). <https://doi.org/10.1109/TIE.2017.2772163>.
- You, F., He, S., Cao, T. & Tang, X. Performance study of a subclass class e power amplifier in comparison with the typical one. In *2008 International Conference on Communications, Circuits and Systems*, 1342–1345 (IEEE, 2008). <https://doi.org/10.1109/ICCCAS.2008.4658014>.
- Jing, M. et al. Atomic superheterodyne receiver based on microwave-dressed Rydberg spectroscopy. *Nat. Phys.* **16**, 911–915 (2020). <https://doi.org/10.1038/s41567-020-0918-5>.
- Cai, M., Xu, Z., You, S. & Liu, H. Sensitivity improvement and determination of Rydberg atom-based microwave sensor. *Photonics* **9**, 250 (2022). <https://doi.org/10.3390/photonics9040250>.
- Ding, D.-S. et al. Enhanced metrology at the critical point of a many-body Rydberg atomic system. *Nat. Phys.* **18**, 1447–1452 (2022). <https://doi.org/10.1038/s41567-022-01777-8>.
- Anderson, D. A., Sapiro, R. E. & Raithe, G. A self-calibrated SI-traceable Rydberg atom-based radio frequency electric field probe and measurement instrument. *IEEE Trans. Antennas Propag.* **69**, 5931–5941 (2021). <https://doi.org/10.1109/TAP.2021.3060540>.
- Sedlacek, J. A. et al. Microwave electrometry with Rydberg atoms in a vapour cell using bright atomic resonances. *Nat. Phys.* **8**, 819–824 (2012). <https://doi.org/10.1038/nphys2423>.
- Meyer, D. H., Castillo, Z. A., Cox, K. C. & Kunz, P. D. Assessment of Rydberg atoms for wideband electric field sensing. *J. Phys. B: At. Mol. Opt. Phys.* **53**, 034001 (2020). <https://doi.org/10.1088/1361-6455/ab6051>.
- Liu, B. et al. Highly sensitive measurement of a megahertz rf electric field with a Rydberg-atom sensor. *Phys. Rev. Appl.* **18**, 014045 (2022). <https://doi.org/10.1103/PhysRevApplied.18.014045>.
- Sayrin, C. et al. Real-time quantum feedback prepares and stabilizes photon number states. *Nature* **477**, 73–77 (2011). <https://doi.org/10.1038/nature10376>.
- Meyer, D. H., Kunz, P. D. & Cox, K. C. Waveguide-coupled Rydberg spectrum analyzer from 0 to 20 GHz. *Phys. Rev. Appl.* **15**, 014053 (2021). <https://doi.org/10.1103/PhysRevApplied.15.014053>.
- Liu, Z.-K. et al. Deep learning enhanced Rydberg multifrequency microwave recognition. *Nat. Commun.* **13**, 1997 (2022). <https://doi.org/10.1038/s41467-022-29686-7>.
- Liu, B. et al. Electric field measurement and application based on Rydberg atoms. *Electromagn. Sci.* **1**, 1–16 (2023). <https://doi.org/10.23919/emsci.2022.0015>.
- Hu, J. et al. Continuously tunable radio frequency electrometry with Rydberg atoms. *Appl. Phys. Lett.* **121**, 014002 (2022). <https://doi.org/10.1063/5.0086357>.

22. Zhang, L.-H. et al. Rydberg microwave-frequency-comb spectrometer. *Phys. Rev. Appl.* **18**, 014033 (2022). <https://doi.org/10.1103/PhysRevApplied.18.014033>.
23. Liu, X.-H. et al. Continuous-frequency microwave heterodyne detection in an atomic vapor cell. *Phys. Rev. Appl.* **18**, 054003 (2022). <https://doi.org/10.1103/PhysRevApplied.18.054003>.
24. Cui, Y. et al. Extending bandwidth sensitivity of Rydberg-atom-based microwave electrometry using an auxiliary microwave field. *Phys. Rev. A* **107**, 043102 (2023). <https://doi.org/10.1103/PhysRevA.107.043102>.
25. Berweger, S. et al. Rydberg-state engineering: investigations of tuning schemes for continuous frequency sensing. *Phys. Rev. Appl.* **19**, 044049 (2023). <https://doi.org/10.1103/PhysRevApplied.19.044049>.
26. Adams, C. S., Pritchard, J. D. & Shaffer, J. P. Rydberg atom quantum technologies. *J. Phys. B: At. Mol. Opt. Phys.* **53**, 012002 (2019). <https://doi.org/10.1088/1361-6455/ab52ef>.
27. Haider, N., Caratelli, D. & Yarovoy, A. G. Recent developments in reconfigurable and multiband antenna technology. *Int. J. Antennas Propag.* **2013**, 869170 (2013). <https://doi.org/10.1155/2013/869170>.
28. Al Abbas, E., Ikram, M., Mobashsher, A. T. & Abbosh, A. Mimo antenna system for multi-band millimeter-wave 5g and wideband 4g mobile communications. *IEEE Access* **7**, 181916–181923 (2019). <https://doi.org/10.1109/ACCESS.2019.2958897>.
29. Cao, Y. F., Cheung, S. W. & Yuk, T. I. A multiband slot antenna for gps/wimax/wlan systems. *IEEE Trans. Antennas Propag.* **63**, 952–958 (2015). <https://doi.org/10.1109/TAP.2015.2389219>.
30. Anderson, D. A., Sapiro, R. E. & Raithel, G. An atomic receiver for am and fm radio communication. *IEEE Trans. Antennas Propag.* **69**, 2455–2462 (2021). <https://doi.org/10.1109/TAP.2020.2987112>.
31. Holloway, C. et al. A multiple-band Rydberg atom-based receiver: Am/fm stereo reception. *IEEE Antennas Propag. Mag.* **63**, 63–76 (2021). <https://doi.org/10.1109/MAP.2020.2976914>.
32. Du, Y. et al. Realization of multiband communications using different Rydberg final states. *AIP Adv.* **12**, 065118 (2022). <https://doi.org/10.1063/5.0095780>.
33. Zou, H. et al. Atomic receiver by utilizing multiple radio-frequency coupling at rydberg states of rubidium. *Appl. Sci.* **10**, 1346 (2020). <https://doi.org/10.3390/app10041346>.
34. Meyer, D. H., Hill, J. C., Kunz, P. D. & Cox, K. C. Simultaneous multiband demodulation using a Rydberg atomic sensor. *Phys. Rev. Appl.* **19**, 014025 (2023). <https://doi.org/10.1103/PhysRevApplied.19.014025>.
35. Mohapatra, A. K., Jackson, T. R. & Adams, C. S. Coherent optical detection of highly excited Rydberg states using electromagnetically induced transparency. *Phys. Rev. Lett.* **98**, 113003 (2007). <https://doi.org/10.1103/PhysRevLett.98.113003>.
36. Šibalić, N., Pritchard, J. D., Adams, C. S. & Weatherill, K. J. Arc: an open-source library for calculating properties of alkali Rydberg atoms. *Comput. Phys. Commun.* **220**, 319–331 (2017). <https://doi.org/10.1016/j.cpc.2017.06.015>.
37. Jau, Y.-Y. & Carter, T. Vapor-cell-based atomic electrometry for detection frequencies below 1 kHz. *Phys. Rev. Appl.* **13**, 054034 (2020). <https://doi.org/10.1103/PhysRevApplied.13.054034>.
38. Bohaichuk, S. M., Booth, D., Nickerson, K., Tai, H. & Shaffer, J. P. Origins of Rydberg-atom electrometer transient response and its impact on radio-frequency pulse sensing. *Phys. Rev. Appl.* **18**, 034030 (2022). <https://doi.org/10.1103/PhysRevApplied.18.034030>.
39. Yang, B. et al. High-sensitive microwave electrometry with enhanced instantaneous bandwidth. Preprint at <https://doi.org/10.48550/arXiv.2310.05008> (2023).
40. Tuchler, M., Schwarz, V. & Huber, A. Location accuracy of an ubw localization system in a multi-path environment. In *2005 IEEE International Conference on Ultra-Wideband*, 414–419 (IEEE, 2005). <https://doi.org/10.1109/ICU.2005.1570023>.
41. Fancher, C. T., Scherer, D. R., John, M.C. S. & Marlow, B.L. S. Rydberg atom electric field sensors for communications and sensing. *IEEE Trans. Quantum Eng.* **2**, 1–13 (2021). <https://doi.org/10.1109/TQE.2021.3065227>.
42. Walker, D. M., Brown, L. L. & Hogan, S. D. Electrometry of a single resonator mode at a Rydberg-atom–superconducting-circuit interface. *Phys. Rev. A* **105**, 022626 (2022). <https://doi.org/10.1103/PhysRevA.105.022626>.
43. Yang, K. et al. Local oscillator port embedded field enhancement resonator for Rydberg atomic heterodyne technique. *EPJ Quantum Technol.* **10**, 23 (2023). <https://doi.org/10.1140/epjqt/s40507-023-00179-w>.
44. Nyquist, H. Thermal agitation of electric charge in conductors. *Phys. Rev.* **32**, 110–113 (1928). <https://doi.org/10.1103/PhysRev.32.110>.
45. Stelzried, C. T. Microwave thermal noise standards. *IEEE Trans. Microw. Theory Tech.* **16**, 646–655 (1968). <https://doi.org/10.1109/TMTT.1968.1126767>.
46. Tu, H.-T. et al. Approaching the standard quantum limit of a Rydberg-atom microwave electrometer. Preprint at <https://doi.org/10.48550/arXiv.2307.15617> (2023).
47. Fancher, C. T., Scherer, D. R., John, M.C. S. & Marlow, B.L. S. Rydberg atom electric field sensors for communications and sensing. *IEEE Trans. Quantum Eng.* **2**, 1–13 (2021). <https://doi.org/10.1109/TQE.2021.3065227>.
48. Santamaria-Botello, G., Verploegh, S., Bottomley, E. & Popovic, Z. Comparison of noise temperature of Rydberg-atom and electronic microwave receivers. Preprint at <https://doi.org/10.48550/arXiv.2209.00908> (2022).
49. Ma, H. F., Shen, X., Cheng, Q., Jiang, W. X. & Cui, T. J. Broadband and high-efficiency conversion from guided waves to spoof surface plasmon polaritons. *Laser Photonics Rev.* **8**, 146–151 (2014). <https://doi.org/10.1002/lpor.201300118>.
50. Jau, Y.-Y. & Carter, T. Vapor-cell-based atomic electrometry for detection frequencies below 1 kHz. *Phys. Rev. Appl.* **13**, 054034 (2020). <https://doi.org/10.1103/PhysRevApplied.13.054034>.

MISCELLANEA

Acknowledgements This work is supported by the National Key R&D Program of China (2022YFA1404002), the National Natural Science Foundation of China (Grant Nos. U20A20218, 61525504, 61722510, 61435011), the Major Science and Technology Projects in Anhui Province (Grant No. 202203a13010001), and the National Natural Science Foundation of China (Grant No. 11934013).

Declaration of Competing Interest The authors declare no competing interests.

© 2024 The Authors. Published by Elsevier B.V. on behalf of Shanghai Jiao Tong University. This is an open access article under the CC BY license (<http://creativecommons.org/licenses/by/4.0/>).